Resistance of domain-wall states in half-metallic CrO$_2$

Wenzhe Chen, Lijuan Qian, and Gang Xiao[*]

Department of Physics, Brown University, Providence, Rhode Island 02912, USA

The half-metallic CrO$_2$ with nearly 100% spin polarization is an ideal system to study magnetic domain-wall resistance, which differs from the resistance (or resistivity) inside a single domain. To experimentally measure the domain-wall resistance, we design and prepare a special CrO$_2$ epitaxial nanostructure with an asymmetrical weak link to localize a domain wall, by using the techniques of chemical vapor deposition and selective-area growth. This structure provides a capability to generate and annihilate a domain wall near the weak link. By contrasting the resistance between a single-domain state and a domain-wall state, we observe a repeatable and reversible resistance jump, namely domain-wall resistance, in half-metallic CrO$_2$. Using the Levy-Zhang model, we further obtain the spin asymmetry ratio $\rho_0^\uparrow/\rho_0^\downarrow$ between resistivities in the two spin channels. The ratio, 4256 ± 388 at 5.0 K, is much larger than that of conventional ferromagnetic metals, attesting to the half metallicity of CrO$_2$.

I. INTRODUCTION

Beyond conventional electronics where electron charges play a dominant role, spintronics has been developed by relying on the electron spins as a memory and logic agent with their distinctive "spin-up" and "spin-down" binary states [1–8]. Among spintronic devices [1], magnetic domain walls (DWs) have been proposed as device elements, for example, in the innovative domain-wall racetrack memory design [9,10]. Some attempts [11–19] have been made to effectively generate DWs and to manipulate or propagate DWs within magnetic nanostructures. The presence of DWs can be probed by a magnetic sensor such as a magnetic tunneling junction [20,21]. Intrinsically, the DW itself is a unique physical object, having its own electronic structure which can differ nontrivially from the corresponding electronic structure of a single-domain ferromagnet. This is particularly so in half-metallic CrO$_2$, where conduction electrons are fully spin polarized, or the minority energy band is completely empty [22–25]. However, within a DW, electron spins are not fully polarized, and there are finite densities of states in both the majority and minority bands. Strictly speaking, the DW region of CrO$_2$ is not a half metal. One natural and basic question is what the resistivity variance is between a single-domain region and a DW region in CrO$_2$. The objective of this project is to measure the domain-wall resistance (DWR) of CrO$_2$, relative to that of the underlying single-domain region.

There have been attempts to measure DWR of various materials such as Co, Fe, Fe/Pt, Co/Pt, (Ga,Mn)As, and SrRuO$_3$ [11–19]. Spin polarizations of common ferromagnetic metals (FMs), Co, Fe, and Ni, are about $42 \sim 46.5\%$ [26,27]. While some DWs contribute positively to the underlying single-domain resistance as expected of the spin texture, some DWs contributes negatively. The latter has been explained

speculatively by the suppression of electron interference in the weakly localized DW region [28]. Levy and Zhang [29] proposed that the admixture of spin states from the magnetization noncollinearity inside a DW leads to an additional resistance. Specifically, the Hamiltonian perturbation from the DW scatters an electron from one spin eigenstate to the other and thus mixes the spin-up and spin-down channels. If the spin-up and spin-down resistivity are the same, i.e., $\rho_0^\uparrow/\rho_0^\downarrow = 1$, spin states admixture from DW makes no contribution to resistance. If two spin channels are very different, particularly in half metal with nearly 100% spin polarization, an interesting question arises: how much will DWR be enhanced? Addressing this question experimentally and theoretically is not only fundamental, but also of significance in the applications of DWs in spintronic devices. For example, probing DWR can be a readout of the racetrack memory or a sensor of the high-frequency dynamical spin states. Unfortunately, little effort has been made to measure the DWR of CrO$_2$, a half metal experimentally confirmed to have the highest spin polarization of nearly 100% [26,30–32]. The primary impediments to this kind of study are the challenges in preparing appropriate epitaxial structure with the necessary probes and the manipulation of DW near the probes. In this work, we present the DWR of CrO$_2$ and the spin asymmetry ratio between the two spin channels. We obtain these results on a uniquely designed epitaxial nanostructure of CrO$_2$, with the capability of DW creation and annihilation within the nanostructure.

II. EXPERIMENT AND CHARACTERIZATION

Due to the nanoscale of DW, experimental measurement of DWR is challenging. Making electrical leads to a DW is not only technically difficult; it can also be invasive to the spin texture of the DW itself. Relative to the size of a sample, the typical DW dimension is on the order of 10 nm, contributing only a tiny volume fraction. The emergence or disappearance of DWR barely registers a noticeable change to the total
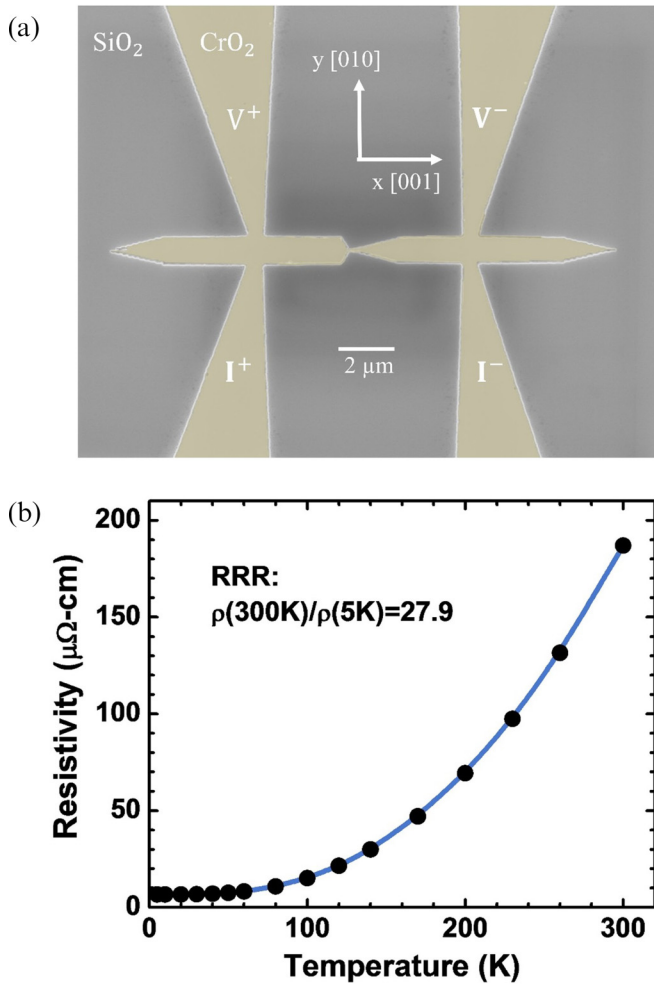
FIG. 1. (a) Scanning electron micrograph of fabricated CrO$_2$ nanostructure sample used in this study (see details in the text). The yellow area is CrO$_2$ and the gray area is SiO$_2$. V$^+$, V$^-$, I$^+$, and I$^-$ labels show the four-point resistance measurement configuration. (b) Characterizing the CrO$_2$ nanostructure sample by measuring its resistivity as a function of temperature between 5.0 and 300.0 K.

resistance (R) of the sample. And, it is this small change that we want to measure and characterize. To overcome this challenge in measuring DWR, we design a nanostructure along the x axis which is also the [001] crystalline axis of CrO$_2$ as shown in Fig. 1(a). The wire (width 1.0 μm $\times$ length 18.0 μm) has two sharp tips at both ends for the purpose of stabilizing the single-domain structure. The center of the wire consists of a narrow constriction, to be referred to as the weak link, so that the DW of the nanostructure is predominantly localized around the weak link. The idea is that, as the DW is generated and annihilated near the weak link, we can measure the DWR with ease. The four contacts along the y axis are integral parts of the sample, serving as current-voltage leads in a four-probe resistance measurement configuration.

This whole CrO$_2$ nanostructure sample is epitaxially grown using a method called selective-area growth [33–35]. The quality of the nanostructure is high, as no postdeposition patterning is needed, and therefore low density of defects in the bulk sample and along the edges is expected. CrO$_2$ grows

epitaxially using chemical vapor deposition (CVD) on single-crystal TiO$_2$, which is our substrate of choice. The sample's geometrical shape is defined lithographically by a thin layer of prepatterned amorphous SiO$_2$ film. The sticking coefficient of CrO$_2$ vapor on SiO$_2$ is null, hence allowing the selective-area growth of CrO$_2$ epitaxial nanostructure. The narrowest neck (or the weak link) of the central constriction is 50 nm and the angles between two edges on the right and left sides are 30° and 120°, respectively. The thickness of our sample is $\sim$100 nm.

We proceed with our sample fabrication process as follows. First, we sputter a 100-nm-thick SiO$_2$ layer on a 5×5-mm^2 rutile TiO$_2$ substrate, followed by spin coating a 200-nm-thick polymethylmethacrylate 950 A4 layer. To prevent charge accumulation on the sample during e-beam lithography, we add a 5-nm-thick Cr layer. Using the FEI Helios$^\circledR$ E-beam Lithographer, we pattern the sample into the intended nanostructure as shown in Fig. 1(a). Afterward, we etch away the unprotected SiO$_2$ layer using reactive ion milling with CHF$_3$ as the reactive gas. Finally, the sample is carefully cleaned and ready for CVD of CrO$_2$. The CVD equipment consists of two furnace zones: a source zone loaded with Cr$_2$O$_3$ precursor maintained at 260 °C and a reaction zone loaded with TiO$_2$ substrate kept at 396 °C. During deposition, we introduce O$_2$ gas as the reactive gas with a flow rate of 100 sccm. The deposition rate is calibrated by using both Dektak$^\circledR$ thickness profilometer and vibrating sample magnetometry. CrO$_2$ has a tetragonal rutile structure with lattice constants of $a = b = 4.421$ Å and $c = 2.916$ Å [33,36]. One parameter to characterize the quality of CrO$_2$ films is the residue resistivity ratio (RRR) = $\rho_{300\,K}/\rho_0$, between room- and low-temperature limit. A large RRR infers insignificant impurity-induced elastic scattering, hence, a low concentration of defects in the sample. Figure 1(b) shows the CrO$_2$ resistivity of the nanostructure sample as a function of temperature from 300.0 to 5.0 K. The residue resistivity is 6.7 $\mu\Omega$ cm at 5.0 K, yielding a RRR of 27.9. This is a rather large ratio, consistent with the published results of high-quality CrO$_2$ epitaxial nanostructures [34,35].

III. DOMAIN-WALL RESISTANCE

We measure the sample resistance as a function of magnetic field to obtain a hysteresis loop of resistance or magnetoresistance (MR) defined as $[R(H_{ext})-R(0)]/R(0)$. Figure 2(a) shows a MR loop within a maximum x-axis field of $\pm$ 50.0 mT at $T = 5.0$ K. Initially, the magnetization direction of CrO$_2$ is made to be along the negative x axis. We then measure the MR, starting from $H_{ext} = 0.0$ to 50.0 mT, then reversing the field and gradually reaching -50.0 mT, finally completing the loop by reversing the field back to the origin of 0 mT. The MR hysteresis loop in Fig. 2(a) reveals a low-resistance state at high fields (± 50.0 mT) and a high-resistance state within 14.6 to 20.2 mT and -14.2 to -21.0 mT. These two states can mutually switch into each other abruptly.

To understand the domain-wall formation and evolution in our nanostructure, we perform micromagnetic simulation of the magnetization state using the software of MUMAX3 [37]. The geometry and size of the simulated entity are the same
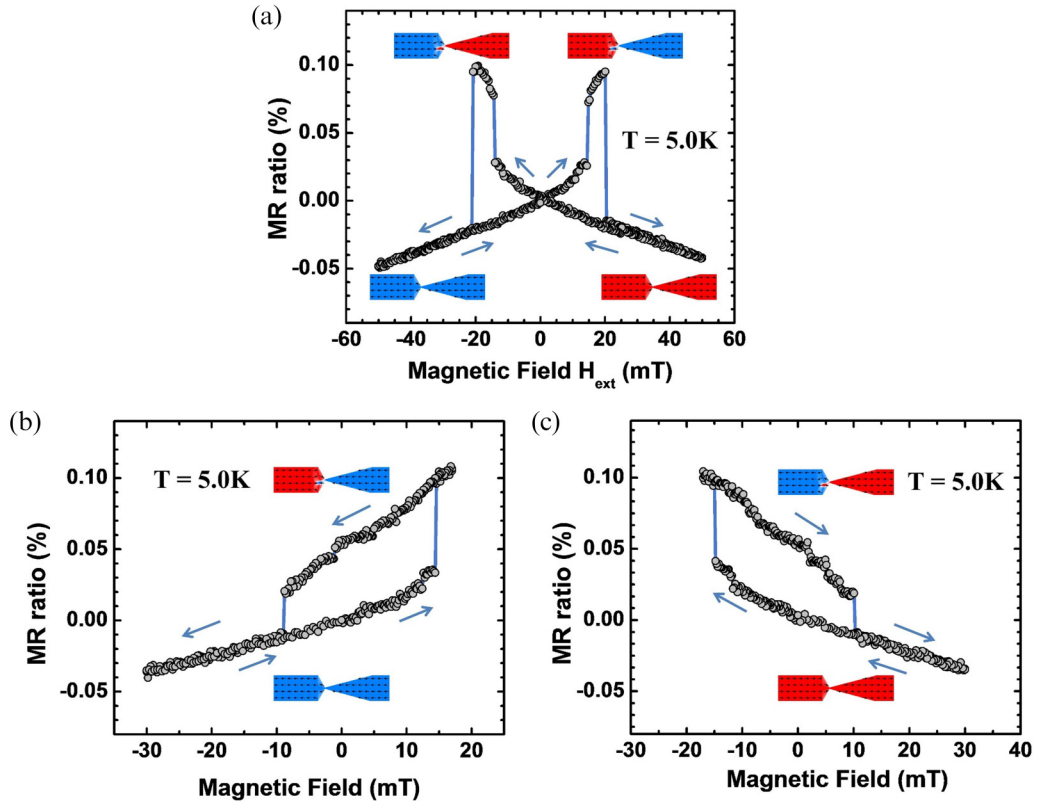
FIG. 2. (a) Magnetoresistance hysteresis loop at 5.0 K of the CrO_2 nanostructure under a sweeping external magnetic field between -50.0 and 50.0 mT along the x axis. The inset magnetization maps are from micromagnetic simulation and the red and blue areas represent magnetization along the positive and negative x axis, respectively. (b) Magnetoresistance hysteresis loop under a sweeping field between -30.0 and 17.0 mT, revealing a low-resistance state of single domain and a high-resistance state of single-domain wall in the nanostructure. (c) Similar to (b), except under a sweeping field between -17.0 and 30.0 mT. The blue arrows are the magnetic-field sweeping direction.

as the real sample, with a cell size of $5 \times 5 \, \text{nm}^2$. The exchange stiffness constant is $A_{ex} = 4.6 \times 10^{-7}$ erg/cm, which is estimated from CrO_2 Curie temperature of $T_C = \sim 390$ K [33]. The uniaxial anisotropy constant for 100-nm CrO_2 film is $K_u = 9.2 \times 10^4$ erg/cm^3 [33]. The simulated multiple distinctive spin maps under different external fields along the x axis are shown in the insets of Fig. 2(a). These spin maps suggest magnetic domain states in our nanostructure under the corresponding field and provide explanation for the abrupt jumps in the MR loops in Fig. 2(a). Let us trace the magnetic domain state as we start at $H_{ext} = -50.0$ mT and gradually increase the field to $+50.0$ through 0 mT. Within the field range, $-50.0 \, \text{mT} \leqslant H_{ext} < 14.6$ mT, the entire nanostructure is a single domain with the magnetization vector aligned along the negative x axis. At the first critical field, $H_{ext} = 14.6$ mT, part of the nanostructure (the left half as suggested by the simulation result) flips its magnetization vector to the positive x axis, creating a DW near the weak link at the center. Further increasing the field to the second critical field, $H_{ext} = 20.2$ mT, causes the whole nanostructure to become a single domain again with the magnetization vector aligned along the x axis. This state is reinforced as the field increases to 50.0 mT. Reversing the field toward -50.0 mT repeats the DW formation process symmetrically and hysteretically. This process is exactly according to our intended purpose of creating a single DW at the weak link and eliminating it

with the help of an external field. The resistance variance between the single-DW configuration and the single-domain state allows us to measure and characterize the DWR.

The MR hysteresis behavior can be understood by analyzing the magnetic domain states under an external field. Our sample has an in-plane uniaxial anisotropy with the x axis ([001]) as the magnetic easy axis [33,35]. At ± 50.0 mT, the whole sample is in a single-domain state with magnetization uniformly aligned along the $\pm x$ axis, respectively. The uniform spin state and suppression of spin fluctuation are possibly responsible for the low resistance observed. The positive/negative slope is determined by the parallel or antiparallel relationship of local magnetization with external field. The slope of the linearity is approximately $\pm 1\%/$T, and this magnitude is consistent with the published result of CrO_2 wire [35,38].

There is another way to create and annihilate a DW state in the nanostructure continuously, as is shown in Figs. 2(b) and 2(c) at $T = 5.0$ K. In Fig. 2(b), we limit the sweeping field within -30.0 and 17.0 mT (versus -50.0 and 50.0 mT). There exists a low-resistance state corresponding to the single-domain state, and a high-resistance state for the single-DW state. Figure 2(b) shows that the nucleation field to create the single-DW state is 14.5 mT, whereas the depinning field to annihilate the single-DW state is -8.9 mT. While in either state, the MR changes smoothly and reversibly with field,
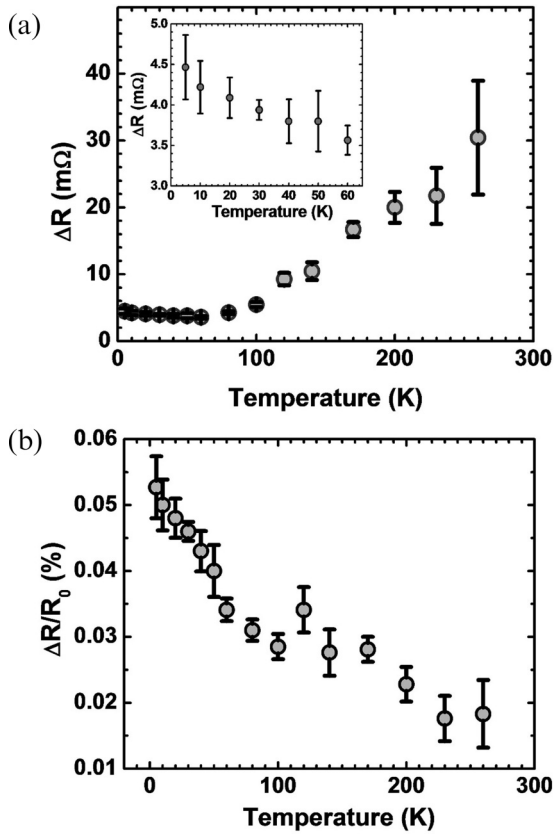
FIG. 3. (a) Temperature dependence of resistance difference ΔR between the high-resistance and the low-resistance state at zero field, obtained from the data shown in Figs. 1(b) and 1(c). The inset is an expanded view of ΔR within 5.0 to 60.0 K. (b) Ratio ($\Delta R/R_0$) of resistance difference ΔR to the zero-field resistance R_0 in the low-resistance single-domain state.

due to a coherent magnetization process under a field. To remove the contribution of the coherent magnetization process, we measure the DW-induced resistance by extracting the total resistance change (ΔR) and MR ($\Delta R/R_0$) of the nanostructure between the single-DW state (with resistance $R_0 + \Delta R$) and the single-domain state (with resistance R_0) at zero magnetic field [11,18,39]. At 5.0 K, the DW-induced ΔR is found to be 4.5 mΩ, and the associated $\Delta R/R_0$ is 0.053%. At each temperature, we measure the MR loop multiple times to provide error analysis. Figure 2(c) is a similar and symmetrical MR loop measured with a sweeping field within -17.0 and 30.0 mT. The shape and amplitude variations are approximately the same between Figs. 2(b) and 2(c), as required by the symmetry of magnetic states under a positive and a negative magnetic field along the x axis.

Figure 3(a) shows ΔR as defined above as a function of temperature from 5.0 to 260.0 K. ΔR is the competing result of two temperature-dependent terms: spin asymmetry and spin disorder. With the increase of temperature, the spin asymmetry is suppressed and the spin disorder increases. Below 60.0 K, ΔR is weakly and linearly dependent on temperature [see details in the inset of Fig. 3(a)]. ΔR is 4.5 $\pm$ 0.4 mΩ at 5.0 K and 3.6 $\pm$ 0.2 mΩ at 60.0 K with a negative linear slope of $(-1.4 \pm 0.2) \times 10^{-2}$ mΩ/K. The spin asymmetry plays an important role, so ΔR decreases with

increasing temperature. Above 60.0 K, ΔR increases suddenly and rapidly with increasing temperature, ultimately reaching as high as 30.4 $\pm$ 8.5 mΩ at 260.0 K. ΔR(260 K) exceeds ΔR(5 K) by a factor of 6.8. In this temperature range, the spin disorder dominates and ΔR increases with increasing temperature. Figure 3(b) shows $\Delta R/R_0$ as defined above as a function of temperature from 5.0 to 260.0 K. $\Delta R/R_0$ is largest (0.053%) at the lowest temperature of 5.0 K, decreasing gradually to 0.034% at 60.0 K, and to 0.018% at 260.0 K.

To determine the intrinsic DWR and get rid of anisotropic magnetoresistance (AMR), we calculate the AMR contribution [38,40] assuming Bloch DW and $\theta =$ arccos[tanh$(\pi x/\sigma_{dw})$] [18,41]:

$$\frac{\Delta R_{\text{AMR}}}{R_0} = \frac{1}{l} \int_{-\infty}^{\infty} \frac{\Delta\rho(\theta)}{\rho_0} dx,$$

where l is wire length of 7.5 μm. For $\Delta R_{\text{AMR}}/R_0$ at low temperature, the magnitude is 0.0014% with a factor of 38 smaller than $\Delta R/R_0$ and the sign is negative, leading to a resistance drop rather than a positive jump in Fig. 2. Similarly, AMR contribution from the rest regions except DW is also neglected.

IV. SPIN ASYMMETRY RATIO

Our micromagnetic simulation shows that the DW is not located along the y axis across the weak link, but rather at the left-hand side of the weak link as illustrated schematically in the inset of Fig. 4. The terminal edges are pinned at the narrowest constriction of the nanostructure. The contour of the DW is approximated as semioval defined by two principal axes as illustrated schematically in the inset of Fig. 4: r is the distance of weak link center to the domain wall and b is the elongation parameter of DW intrusion to the left half of the nanostructure. Considering the possible deviation of real domain wall from our simulated spin configuration, we base our analysis on different shape of the DW contour, i.e., the b/r ratio. the DW resistivity ratio ($\Delta\rho_{\text{DW}}/\rho_0$) and the experimentally measured $\Delta R/R_0$ ratio obeys the following
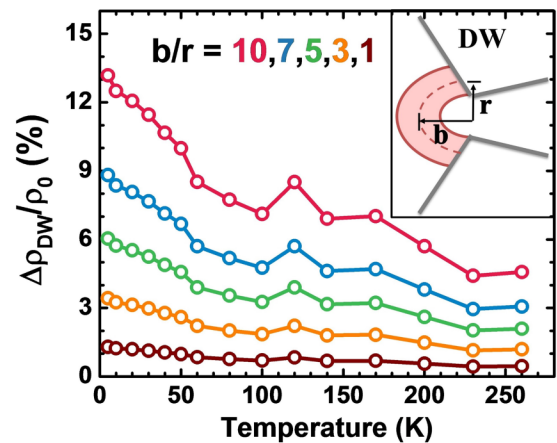
FIG. 4. Ratio of DW resistivity to the longitudinal resistivity based on different shape of domain-wall contour b/r. $b/r = 5$ is the approximated value obtained from micromagnetic simulation. The inset shows the domain-wall contour shape.

relationship,

$$\Delta\rho_{DW}/\rho_0 = \beta \times \Delta R/R_0,$$

where β is a constant factor dependent on b/r. For CrO_2, the domain wall width $\delta_{DW} = \pi\sqrt{A/K_u}$ is estimated to be 70.2 nm. Figure 4 shows $\Delta\rho_{DW}/\rho_0$ versus different temperature based on different DW contour shape (b/r). Assuming a semicircle contour ($\beta = 24.7$), $\Delta\rho_{DW}/\rho_0$ is 1.30% at 5.0 K, 0.84% at 60.0 K, and 0.45% at 260.0 K. However, a large elongated contour with $b/r = 10$ ($\beta = 249.8$), $\Delta\rho_{DW}/\rho_0$ would be 13.18% at 5.0 K, 8.52% at 60.0 K, and 4.57% at 260.0 K.

According to the theory of Levy and Zhang [29], the DWR arises from the mixture of resistivities in the two spin channels, the spin-up channel $\rho_0^\uparrow$ and the spin-down channel $\rho_0^\downarrow$. For current parallel to domain walls (CIW) and current perpendicular to domain wall (CPW), DW resistivity ratio is given by the following formula, respectively:

$$\frac{\Delta\rho_{CIW}}{\rho_0} = \frac{\xi^2}{5}\frac{(\alpha-1)^2}{\alpha},$$

$$\frac{\Delta\rho_{CPW}}{\rho_0} = \frac{\xi^2}{5}\frac{(\alpha-1)^2}{\alpha}\left(3 + \frac{10\sqrt{\alpha}}{\alpha+1}\right),$$

where $\xi = \pi\hbar^2 k_F/4mJ\delta_{DW}$ and $\alpha = \rho_0^\uparrow/\rho_0^\downarrow$. For CrO_2, the Fermi wave vector k_F is 1 Å^{-1}; Stoner exchange splitting J is 1.8 eV. Since charge current flows primarily perpendicular to the DW, the second formula is applicable in our case. Using the values of $b/r = 5$ and $\beta = 114.4$, estimated from the simulated domain-wall configuration, we calculate that the values of $\Delta\rho_{DW}/\rho_0$ and $\rho_0^\uparrow/\rho_0^\downarrow$ are 6.04% and 4256 ± 388 at 5.0 K, 3.90% and 2719 ± 141 at 60.0 K, 2.09% and 1428 ± 416 at 260.0 K, respectively. These are very large values comparative to conventional ferromagnets (non-half metals). For example, $\rho_0^\uparrow/\rho_0^\downarrow$ in Co films is estimated in the range of 5–20 at room temperature [14,29]. For Ni and Fe, $\rho_0^\uparrow/\rho_0^\downarrow$ is on the order of 10 at low temperature and 1 at room temperature [42]. The spin resistivity asymmetry of $L1_0$ FePd is about 12 at 50 K and decreases to about 3 at room temperature [43]. The $\rho_0^\uparrow/\rho_0^\downarrow$ ratio in half-metal CrO_2 is larger than that in non-half metals by 2 to 3 orders of magnitude. $\rho_0^\uparrow/\rho_0^\downarrow$ decreases approximately linearly with increasing temperature. Strictly speaking, a half metal is a zero-temperature concept. At a finite temperature, the generation of spin waves creates increasing density of states in the minority band, hence reducing the $\rho_0^\uparrow/\rho_0^\downarrow$ ratio.

V. CONCLUSION

In conclusion, we report an observation of DWR in half-metallic CrO_2 by employing two types of magnetoresistance hysteresis loop: full loop and half loop. In our asymmetrical nanostructure, the field to generate a domain wall is consistent and stable. Sweeping the magnetic field along the nanostructure at a critical field annihilates the domain wall. By measuring the resistance jump between the single-domain state and the single-DW state, we are able to extract the resistance difference within DW in nature's ultimate half metal CrO_2. Further analysis presents a very large spin asymmetry in the resistivity ratio between the majority and the minority spin channels. We provide our electron transport results within the domain-wall region over a broad temperature range of 5.0 to 260.0 K. These results may offer insight into the theoretical understanding of the effect of magnons at finite temperatures on the integrity of the half-metallic state.

[1] J. Sinova, S. O. Valenzuela, J. Wunderlich, C. H. Back, and T. Jungwirth, Rev. Mod. Phys. **87**, 1213 (2015).

[2] I. Žutić, J. Fabian, and S. Das Sarma, Rev. Mod. Phys. **76**, 323 (2004).

[3] L. Liu, C.-F. Pai, Y. Li, H. W. Tseng, D. C. Ralph, and R. A. Buhrman, Science **336**, 555 (2012).

[4] Q. Hao, W. Chen, and G. Xiao, Appl. Phys. Lett. **106**, 182403 (2015).

[5] W. Chen, G. Xiao, Q. Zhang, and X. Zhang, Phys. Rev. B **98**, 134411 (2018).

[6] I. M. Miron *et al.*, Nature (London) **476**, 189 (2011).

[7] W. Chen, L. Qian, and G. Xiao, Sci. Rep. **8**, 8144 (2018).

[8] W. Chen, L. Qian, and G. Xiao, AIP Adv. **8**, 055918 (2018).

[9] S. S. Parkin, M. Hayashi, and L. Thomas, Science **320**, 190 (2008).

[10] D. A. Allwood, G. Xiong, C. Faulkner, D. Atkinson, D. Petit, and R. Cowburn, Science **309**, 1688 (2005).

[11] U. Ebels, A. Radulescu, Y. Henry, L. Piraux, and K. Ounadjela, Phys. Rev. Lett. **84**, 983 (2000).

[12] D. Buntinx, S. Brems, A. Volodin, K. Temst, and C. Van Haesendonck, Phys. Rev. Lett. **94**, 017204 (2005).

[13] U. Rüediger, J. Yu, S. Zhang, A. D. Kent, and S. S. P. Parkin, Phys. Rev. Lett. **80**, 5639 (1998).

[14] J. F. Gregg, W. Allen, K. Ounadjela, M. Viret, M. Hehn, S. M. Thompson, and J. M. D. Coey, Phys. Rev. Lett. **77**, 1580 (1996).

[15] R. Danneau *et al.*, Phys. Rev. Lett. **88**, 157201 (2002).

[16] C. Hassel, M. Brands, F.-Y. Lo, A. D. Wieck, and G. Dumpich, Phys. Rev. Lett. **97**, 226805 (2006).

[17] H. Tang, S. Masmanidis, R. Kawakami, D. Awschalom, and M. Roukes, Nature (London) **431**, 52 (2004).

[18] D. Chiba, M. Yamanouchi, F. Matsukura, T. Dietl, and H. Ohno, Phys. Rev. Lett. **96**, 096602 (2006).

[19] L. Klein, Y. Kats, A. F. Marshall, J. W. Reiner, T. H. Geballe, M. R. Beasley, and A. Kapitulnik, Phys. Rev. Lett. **84**, 6090 (2000).

[20] J. Hayakawa, S. Ikeda, F. Matsukura, H. Takahashi, and H. Ohno, Jpn. J. Appl. Phys. **44**, L587 (2005).

[21] X. Liu, W. Zhang, M. J. Carter, and G. Xiao, J. Appl. Phys. **110**, 033910 (2011).

[22] S. P. Lewis, P. B. Allen, and T. Sasaki, Phys. Rev. B **55**, 10253 (1997).

[23] L. Chioncel, H. Allmaier, E. Arrigoni, A. Yamasaki, M. Daghofer, M. I. Katsnelson, and A. I. Lichtenstein, Phys. Rev. B **75**, 140406 (2007).

[24] K. Schwarz, J. Phys. F: Met. Phys. **16**, L211 (1986).

[25] M. I. Katsnelson, V. Y. Irkhin, L. Chioncel, A. I. Lichtenstein, and R. A. de Groot, Rev. Mod. Phys. **80**, 315 (2008).

[26] R. Soulen *et al.*, Science **282**, 85 (1998).

[27] Q. Hao, W. Chen, S. Wang, and G. Xiao, J. Appl. Phys. **122**, 033901 (2017).

[28] G. Tatara and H. Fukuyama, Phys. Rev. Lett. **78**, 3773 (1997).

[29] P. M. Levy and S. Zhang, Phys. Rev. Lett. **79**, 5110 (1997).

[30] Y. Ji, G. J. Strijkers, F. Y. Yang, C. L. Chien, J. M. Byers, A. Anguelouch, G. Xiao, and A. Gupta, Phys. Rev. Lett. **86**, 5585 (2001).

[31] J. S. Parker, S. M. Watts, P. G. Ivanov, and P. Xiong, Phys. Rev. Lett. **88**, 196601 (2002).

[32] A. Anguelouch, A. Gupta, G. Xiao, D. W. Abraham, Y. Ji, S. Ingvarsson, and C. L. Chien, Phys. Rev. B **64**, 180408 (2001).

[33] G. Miao, G. Xiao, and A. Gupta, Phys. Rev. B **71**, 094418 (2005).

[34] X. Zou, G. Xiao, S. Huang, T. Chen, and C.-L. Chien, J. Appl. Phys. **103**, 07D701 (2008).

[35] X. Zou and G. Xiao, Phys. Rev. B **77**, 054417 (2008).

[36] X. Li, A. Gupta, and G. Xiao, Appl. Phys. Lett. **75**, 713 (1999).

[37] A. Vansteenkiste, J. Leliaert, M. Dvornik, M. Helsen, F. Garcia-Sanchez, and B. Van Waeyenberge, AIP Adv. **4**, 107133 (2014).

[38] C. König, M. Fonin, M. Laufenberg, A. Biehler, W. Bührer, M. Kläui, U. Rüdiger, and G. Güntherodt, Phys. Rev. B **75**, 144428 (2007).

[39] A. von Bieren, A. K. Patra, S. Krzyk, J. Rhensius, R. M. Reeve, L. J. Heyderman, R. Hoffmann-Vogel, and M. Kläui, Phys. Rev. Lett. **110**, 067203 (2013).

[40] M. S. Anwar and J. Aarts, Phys. Rev. B **88**, 085123 (2013).

[41] M. Viret, Y. Samson, P. Warin, A. Marty, F. Ott, E. Søndergård, O. Klein, and C. Fermon, Phys. Rev. Lett. **85**, 3962 (2000).

[42] A. Fert and I. A. Campbell, J. Phys. F: Met. Phys. **6**, 849 (1976).

[43] C. H. Marrows and B. C. Dalton, Phys. Rev. Lett. **92**, 097206 (2004).